Nanostructured Thermionics for Conversion of Light to Electricity: Simultaneous Extraction of Device Parameters

Amir H. Khoshaman, Andrew T. Koch, Mike Chang, Harrison D. E. Fan, Mehran Vahdani Moghaddam, and Alireza Nojeh

***Abstract*—Thermionic conversion involves the direct conversion of heat, including light-induced heat, from a heat source, e.g., solar energy, to electricity. Although the concept is almost a hundred years old, the progress of thermionic convertors has been limited by issues such as the space-charge effect and availability of materials with desirable mechanical and electrical properties, while maintaining a low work function. Nanotechnology could help address some of the main challenges that thermionic convertors face. However, existing models, which were developed for macroscopic convertors, are not capable of describing all aspects of nanostructured devices. We present a method to evaluate the output characteristics of thermionic convertors with a higher precision than the existing models and the ability to simulate a broader range of parameters, including temperatures, active surface areas, interelectrode distances, and work functions. These features are crucial for the characterization of emergent devices due to the unknowns involved in their internal parameters; the model's high numerical precision and flexibility allows one to solve the reverse problem and to evaluate the internal parameters of the device from a set of simple experimental data. As an experimental case, a carbon nanotube forest was used as the emitter and locally heated to thermionic emission temperatures using a 50-mW-focused laser beam. The current–voltage characteristics were measured and used to solve the reverse problem to obtain the internal parameters of the device, which were shown to be consistent with the values obtained using other methods.**

***Index Terms*—Carbon nanotubes, light induced thermionic emission, thermionic emission, thermionic conversion, Vlaslov's equation.**

I. Introduction

PHOTOVOLTAIC devices use optical generation of charge carriers. Thermionic energy convertors (TECs), on the other hand, employ heat, which could also be generated by light, and act as a heat engine without moving parts to generate electricity by means of thermionic emission.

Manuscript received November 5, 2014; accepted April 21, 2015. Date of publication April 24, 2015; date of current version July 7, 2015. This work was supported by the Natural Sciences and Engineering Research Council, the Canada Foundation for Innovation, the British Columbia Knowledge Development Fund, the BCFRST Foundation, the British Columbia Innovation Council, the University of British Columbia, and the Peter Wall Institute for Advanced Studies.

The authors are with the Department of Electrical and Computer Engineering, University of British Columbia, Vancouver, BC V6T 1Z4, Canada (e-mail: akhosham@ece.ubc.ca; akoch@ece.ubc.ca; hungc@ece.ubc.ca; harrison@ece.ubc.ca; mehranvm@ece.ubc.ca; anojeh@ece.ubc.ca).

Color versions of one or more of the figures in this paper are available online at http://ieeexplore.ieee.org.

Digital Object Identifier 10.1109/TNANO.2015.2426149

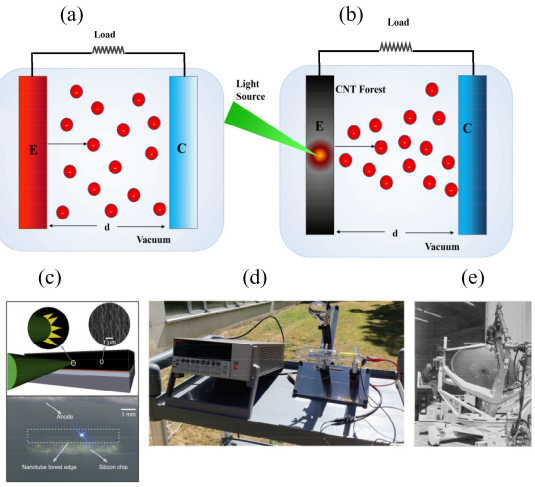

Fig. 1. Schematic diagram of (a) a traditional TEC, (b) a LITEC based on CNT forests. (Reprinted from [15] with permission from Elsevier.) (c) As the intensity of the incident light is increased beyond a threshold value, an incandescent glow emerges [5]. (d) A CNT-based LITEC device in a portable sealed glass vacuum chamber [13] as opposed with (e) the large focusing infrastructure required for traditional LITEC devices [3] (with permission from AIP Publishing LLC).

The thermionic emission phenomenon has been known for a long time: it was reported by Guthrie [1] and by Edison [2]. The effect was quantified by Richardson [3].

Generally, TECs consist of two electrodes separated by a vacuum gap as depicted in Fig. 1(a). Electrons are thermionically ejected into the vacuum region from the hot emitter, traverse the gap and are collected by the cold collector. These devices offer attractive properties for harvesting the solar energy, such as the exponential dependence of current density on temperature and the ability to harness a wide spectral range of the incident light.

TECs have been used in the last 50 years for direct conversion of heat to electricity. However, there has been a recent surge of interest in this field due to two main reasons: the ever-increasing need for generation of clean energy, as well as the advances in nanotechnology enable researchers to overcome some of the main challenges associated with traditional TECs. Some of the latest advances in the field of thermionic convertors include workfunction reduction by means of intercalation of nanostructured cathodes [4]–[6], negative electron affinity materials [7], photon-enhanced thermionic emission [8], and application of magnetic fields [9] or extremely small interelectrode distances [10] to increase efficiency.

An overview of the new prospects for thermionic conversion offered by nanotechnology is given in Ref. [11].

Due to their high-temperature and mechanical stability, carbon nanotubes (CNTs) are viable candidates for thermionic emission [12] and energy conversion applications [13]. Due to thermal dissipation in bulk conductors, light induced thermionic emission (LITE) requires very high optical powers, obtainable for example, by using a large and complex apparatus to focus and collect sunlight as shown in Fig. 1(e) [14]. In particular, the heating situation can be drastically different in nanotube-based cathodes compared to bulk conductors. Our group has previously reported light-induced localized heating in multi-wall carbon nanotubes (MWCNT) forests [15]. This "Heat Trap effect" enables localized heating to temperatures above 2000 K using a low-power beam of visible light, leading to localized thermionic electron emission as depicted in Fig. 1(b)–(c). Based on this effect, our group has subsequently demonstrated a vacuum thermionic convertor (see Fig. 1(d)), [13].

Upon light-induced heating of the emitter, the electrons in the high-energy Fermi tail have enough energy to overcome the workfunction barrier. These electrons are ejected from the surface of the emitter and traverse the inter-electrode distance to finally reach the cold collector. The difference between the electrochemical potential energies of the two electrodes is transformed into work in the external load through which the electrons travel back to the emitter.

Hatsopoulos and Gyftopoulos proposed a method to couple Vlaslov's and Poisson's equations in the space-charge limited regime, assuming the electrons in the interelectrode space act as a collisionless gas with a Boltzmann velocity distribution [16]–[17]. This method can be used to evaluate the current–voltage (*I–V*) characteristics in the space-charge limited mode of thermionic convertors. However, this strategy has never been used to solve the reverse problem and to obtain the internal parameters of the device from the *I–V* curves. This is because conventional thermionic devices are made using metal electrodes with known properties, such as workfunction, and the entire electrode is typically heated; parameters such as emission spot area are well known and temperature can be easily measured. Therefore, Hatsopoulos and Gyftopoulos assumed a uniform temperature profile in their model [16], [17]. However, as will be shown in this paper, a large temperature gradient may exist in nanomaterial-based thermionics. For instance, in a CNT-based light induced thermionic energy convertor (LITEC), only a small portion (with a radius, *r*, on the order of several hundred micrometers) of the nanotube array may be heated. The exact value of the workfunction depends on the local properties and temperature of the illuminated spot [18]. Moreover, the presence of adsorbates can have noticeable effects on the workfunction of CNTs. For instance, the adsorption of water molecules will reduce the workfunction [19]–[20] while the presence of organic molecules on the CNT tip will result in larger workfunctions [18]. Additionally, the local density of states at the tip and sidewalls of CNTs are different, leading to different values of workfunctions [21].

Therefore, the study of these emerging thermionic devices requires a strategy to characterize their internal parameters. In addition, the lack of sufficient computational power and a stable algorithm have made it difficult to tackle the more computationally intensive, reverse problem in the past. The integrals involved in this method do not have exact analytical solutions and behave non-linearly as the internal parameters of the device are varied. In fact, the numerical approximations tabulated in Ref. [16] are sufficient to predict the space-charge limited behaviour of thermionic convertors only in a limited range of temperatures, workfunctions, and interelectrode spacings.

II. Theory and Model

It is assumed that electrons are thermionically emitted from the cathode as governed by the Richardson–Dushman equation, $J_{sat} = AT_E^2 \exp(-\phi_E/k_B T_E)$, where J_{sat} denotes the saturation current density, i.e., the maximum current density attainable from the emitter at the emitter's temperature, $T_E \cdot k_B$ is the Boltzmann constant, and $A = 1.202 \times 10^6 \,\mathrm{A} \cdot \mathrm{m}^{-2} \cdot \mathrm{K}^{-2}$ is the Richardson–Dushman constant [22].

The electrons reaching the other electrode (collector or anode) are completely collected and run through the external circuit. The methodology in this section follows the earlier description of operation of TECs in the space-charge limited regime [6], [17]. It is described here how the numerical accuracy and the range of applicability can be further enhanced using a new algorithm. Moreover, the *I–V* characteristics of the TEC are obtained for different regimes of device operation. The high numerical accuracy, applicability to a wide range of parameters, and modelling of the entire *I–V* characteristics, in addition to a stable algorithm, make solving the more challenging reverse problem possible. The general method to solve the direct problem is to couple Poisson's and Vlaslov's equations. Vlaslov's equation applies when electrons in the interelectrode region are approximated as a collisionless ideal gas [23]. In the simplest one-dimensional (1-D) case, i.e., when a uniform electric field is applied only in the direction normal to the emitter and collector's surface (e.g., along the *x*-axis), an analytical solution is possible. The solution includes functions and integrals that can be solved numerically. The operation of the TECs in the space-charge mode is discussed in Ref. [17]. We provide a summary of the key points along with important equations for the sake of clarity. We also propose an algorithm that can be utilized to increase the accuracy of the method proposed in Ref. [16] to calculate the *I–V* characteristics.

A TEC can operate in two or three distinct regimes (or modes), depending on the electric potential difference between the electrodes (see Fig. 2). The width of each mode and the onset of the subsequent mode depend on the internal parameters of the TEC such as temperature, interelectrode gap distance, and the workfunctions. Fig. 2(a) shows the *I–V* characteristics of a typical TEC in its various operating regimes. The appropriate motive diagrams that are the analogs of the band-diagrams in solid state physics are also included. The emitter and collector are assumed to have the same Richardson–Dushman constant and maintained at T_E and T_C, respectively. The motive diagram of a TEC operating under negative and positive biases is depicted in Fig. 2(b) and (c).

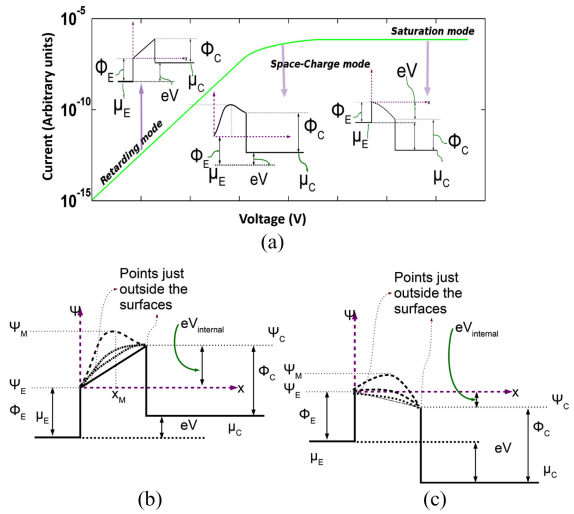

Fig. 2. (a) A typical *I–V* curve with the corresponding motive diagrams in each operation regime. (b), (c) Typical motive diagrams corresponding to different operation regimes of a vacuum thermionic convertor under negative (b) and positive biases (c). The subscripts "E" and "C" denote emitter and collector, respectively. Ψ, μ and ϕ denote the motive, electrochemical potentials and workfunctions, respectively.

At sufficiently negative biases, where the chemical potential of the emitter lies considerably below that of the collector, the device is in the retarding mode. The electric field opposes the transport of electrons from the emitter toward the collector and only a fraction of them with sufficient kinetic energy to overcome the electrostatic barrier can make it to the other side. Therefore, the current in this regime can be calculated as $J = AT_E^2 \exp(-(\phi_C + eV)/k_B T_E)$. It is noted that in this mode, due to the low concentration of electrons, the electron-electron interaction is negligible and, therefore, not included in the calculations. In other words, all electrons are assumed to be subject to the same opposing electric field in the inter-electrode gap; the spatial changes of the field due to the presence of electrons in the inter-electrode region are not considered.

As the concentration of electrons rises by lowering the potential energy of the collector with respect to that of the emitter, the electric field arising from the presence of electrons in the inter-electrode region must be taken into account. The electrons ejected from the emitter effectively face a higher local potential barrier due to the electrostatic repulsion arising from the other electrons. This characterizes the space-charge limited regime. As observed from Fig. 2, the presence of the electrons in this region results in a peak in the inter-electrode potential ($\psi = \psi_M$ at position $x = x_M$). Electrons situated between the surface of the emitter and x_M can have both positive and negative velocities. Only those electrons with kinetic energy equal to or greater than ψ_M are able to pass over the maximum potential. On the other hand, once electrons overcome ψ_M, their potential energy only decreases for values of x higher than x_M. Consequently, they can only drift toward the collector.

As the applied bias increases, x_M moves consistently toward the emitter and, eventually, ψ_M does not take place in the inter-electrode gap. The device has entered the saturation mode. The current density in this case is equal to J_{sat} and remains constant by increasing the electric field. This approximation is valid for relatively low applied biases, whereas the Schottkey effect becomes important at higher biases, whereas the effective work-function is lowered according to $\phi_{eff} = \phi_E - \sqrt{\frac{e^3 F}{4\pi\varepsilon_0}}$, where ε_0 is the vacuum constant and F is the magnitude of the electric field [24]–[25].

A. Space-charge Limited Regime

The space-charge limited regime is characterized by two boundary points. The onset of the space-charge limited regime, where ψ_M takes place at the point just outside the collector, is known as the critical voltage. This point is denoted by J_C and V_C as the critical current density and applied voltage, respectively. On the other hand, when ψ_M coincides with the point just outside the emitter, the device is at the saturation point. This point is identified by J_{sat} and V_{sat}.

In order to obtain the overall *I–V* characteristics, the saturation current and voltage are determined. Then, as explained in the following section, the critical point is evaluated. The values of the current and voltage between these two boundaries are subsequently computed from coupling Vlaslov's and Poisson's equations. Starting with a current, Vlaslov's equation outputs the velocity distribution function, $f(x, v_e)$. The electron density as a function of x, $n(x)$ is evaluated by integrating $f(x, v_e)$. The resulting $n(x)$ is plugged into Poisson's equation. The solution to Poisson's equation can be evaluated numerically to obtain the bias particular to that current.

1) Theory of the Space-Charge Limited Regime: In order to calculate the characteristics in the space-charge limited mode, the electron velocity distribution function, $f(x, v_e)$, the electron number density, $n(x)$, and the dimensionless Poisson's equations are obtained and solved numerically. In the case of collisionless electrons, Vlaslov's equation can be solved to determine the distribution function of electrons.

At x_M, the distribution function, $f(x_M, v_e)$ takes the form of a half-Maxwellian at temperature T_E; i.e., for $v_{ex} > 0$, the distribution is Maxwellian, whereas for $v_{ex} < 0$, the distribution is zero. v_{ex} represents the velocity of the electron along the *x* direction. The equation for $f(x_M, v_e)$ can be used as the boundary condition to calculate the distribution function. Within the region $x > x_M$, in Fig. 2, the electrons are accelerated by the negative space-charge since the gradient of the motive is always negative. The minimum value of the velocity at point x, i.e., $v_{ex,min}$, is therefore equal to the velocity component of electrons starting with zero initial velocity at x_M. Consequently these electrons undergo a motive difference of $\psi_M - \psi(x)$ corresponding to $v_{ex,min} = (2\frac{\psi_M - \psi(x)}{m})^{1/2}$ and, therefore, when $x > x_M$ solution to the Vlaslov's equation is equal to

$$f(x, v_e) = 2n(x_M)\left(\frac{m}{2\pi k_B T_E}\right)^{\frac{3}{2}} \times \exp\left(\frac{\psi_M - \psi(x)}{k_B T_E} - \frac{m v_e^2}{2 k_B T_E}\right) \times \Theta\left(v_{ex} - (v_{ex})_{min}\right), \quad (1a)$$

where m is the mass of the electron, $v_e = (v_{ex}^2 + v_{ey}^2 + v_{ez}^2)^{1/2}$ is the electron speed, and Θ is the Heaviside step function.

On the other hand, at $x < x_M$, the electrons are decelerated by the electric field and can have both positive and negative velocities along the x direction. This leads to a negative minimum velocity along the x direction, $v_{ex,min} = -(2\frac{\psi_M - \psi(x)}{m})^{1/2}$. Therefore, when $x \le x_M$, the velocity distribution function is given by

$$f(x, v_e) = 2n(x_M)\left(\frac{m}{2\pi k_B T_E}\right)^{\frac{3}{2}} \times \exp\left(\frac{\psi_M - \psi(x)}{k_B T_E} - \frac{m v_e^2}{2 k_B T_E}\right) \times \Theta\left(v_{ex} + (v_{ex})_{min}\right). \quad (1b)$$

Based on this explanation, electrons on either side of x_M also take on a half-Maxwellian velocity distribution with the peak shifted from 0 to $v_{x,min}$. The next step is to calculate the electron number density, $n(x)$, by integration of the velocity distribution function over the entire velocity space at x. This results in

$$n(x) = n(x_M)\exp(\gamma)\begin{cases} 1 - \operatorname{erf}\left(\gamma^{1/2}\right), & x > x_M \\ 1 + \operatorname{erf}\left(\gamma^{1/2}\right), & x \le x_M \end{cases} \quad (2)$$

where $\gamma \equiv (\psi_M - \psi(x))/k_B T_E$ is the dimensionless potential and erf is the error function.

In order to obtain the dimensionless Poisson's equation, x is divided by the Debye length given by $L_{\mathrm{D}} \equiv (\frac{\varepsilon_0 k_B T_E}{2e^2 n_e(x_M)})^{\frac{1}{2}}$ [23]. The resulting equation is

$$\frac{d^2\gamma}{d\zeta^2} = \frac{1}{2}\exp(\gamma) \times \begin{cases} 1 - \operatorname{erf}\left(\gamma^{1/2}\right), & \zeta \ge 0 \\ 1 + \operatorname{erf}\left(\gamma^{1/2}\right), & \zeta < 0 \end{cases} \quad (3)$$

where $\zeta \equiv (x - x_M)/L_{\mathrm{D}}$ is the dimensionless distance. Noting that ψ_M is a stationary point of $\psi(x)$, the corresponding boundary conditions are obtained as $\gamma_{(\zeta=0)} = 0$ and $(\frac{d\gamma}{d\zeta})_{(\zeta=0)} = 0$. Double-integrating the equation and utilizing the boundary conditions lead to

$$\zeta = -\int_0^{\gamma} \frac{d\alpha}{\left[\exp(\alpha) + \exp(\alpha)\operatorname{erf}\left(\alpha^{\frac{1}{2}}\right) - 2\left(\frac{\alpha}{\pi}\right)^{\frac{1}{2}} - 1\right]^{1/2}} \quad (4a)$$

for $\zeta < 0$ and

$$\zeta = \int_0^{\gamma} \frac{d\alpha}{\left[\exp(\alpha) - \exp(\alpha)\operatorname{erf}\left(\alpha^{\frac{1}{2}}\right) + 2\left(\frac{\alpha}{\pi}\right)^{\frac{1}{2}} - 1\right]^{1/2}} \quad (4b)$$

for $\zeta > 0$.

The integral on the right hand side of equation (4) was solved numerically with higher precision and with three orders of magnitude of wider range compared to [16], as plotted in Fig. 3(a). As depicted in Fig. 3(b), having a limited range for the dimensionless variables and using interpolation as prescribed in Ref. [16], can lead to substantial errors.

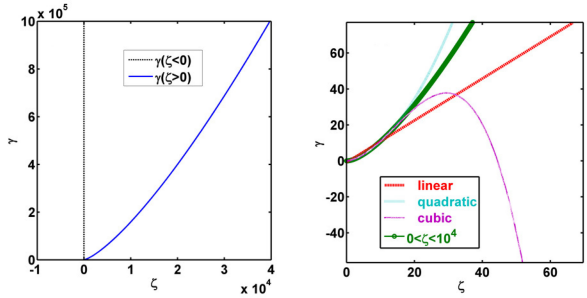

Fig. 3. (a) The dimensionless motive (γ) vs. dimensionless distance (ζ) plotted as the solution of the coupled Poisson and Vlaslov equations. (b) The values of the dimensionless motive, γ are fitted using linear, quadratic and cubic polynomial functions in the range $0 < \zeta < 15$, as tabulated in Ref. [6]. These fitted polymonials are used to extrapolate the values of γ for $\zeta > 15$. As observed, having a limited range for dimensionless motive leads to substantial deviations from the actual solutions in case that a limited range of the values of the dimensionless variables are used.

A high precision and a wide range for the values of the dimensionless motive and distance are imperative in order to be able to solve the reverse problem and extract the device parameters from the experimental *I–V* curves. The calculation of the values of the integrals in equation (4) requires dealing with functions that change drastically depending on the values of α. Furthermore, the limits of integration involve large numbers (the values of γ), growing ever larger once used as inputs to exponential functions. The values of ζ for $0 < \gamma < 14$ are tabulated in Ref. [16]. The existing strategy was to extrapolate these values to the desired specifications of the device. However, as will be shown in the following section, the extrapolated values obtained by fitting to different polynomials do not lead to desirable accuracy at higher values of ζ. The greatest error arises in determination of the values of the critical current and voltage. In order to evaluate the integrals, the variable-precision arithmetic feature from MATLAB's Symbolic Math Toolbox was employed to compute each element to at least seven significant digits of accuracy. After calculating the integrals numerically, it was noticed that for $\zeta_C > 10$, γ can be fitted to a three-term function in the form $\gamma_C = a\zeta_C^b + c + e\zeta_C^d$, where $a = 0.7388$, $b = 1.333$, $c = 2.198$, $d = 0.6712$ and $e = -1.476$, with a root mean square error (RMSE) of 1.144. Moreover, for $\zeta_E > 2$, $\zeta_E = a\exp(-b\gamma_E) + c$, where $a = -1.497, b = 0.5125, c = 2.554$, and $RMSE = 0.0004346$.

The value of the current density can be calculated by integrating $ef(x, v_e)v_{ex}$ at any arbitrary $0 < x < d$, (d being the interelectrode distance) over the entire velocity space. The result is $J = en(x_M)(\frac{2k_B T_E}{\pi m})^{1/2}$. This equation can be used to replace $n(x_M)$ in the definition of Debye length and directly relate it to the current as $L_D = (\frac{\varepsilon_0^2 k_B^3}{2\pi m e^2})^{\frac{1}{4}} \frac{T_E^{3/4}}{J^{1/2}}$.

The final step is to link J to the maximum current density obtainable from the emitter, i.e., J_{sat}, by calculating the number of electrons with $v_x > 0$ at the point just outside the emitter. In other words, $J = J_{sat}$ when $x_M = 0$. This leads to $J_{sat} = J\exp(\gamma_E)$, where $\gamma_E = \gamma(x = 0)$. Based on these equations and values from Fig. 3(a), the following procedure is proposed to obtain the *I–V* characteristics of the entire device.

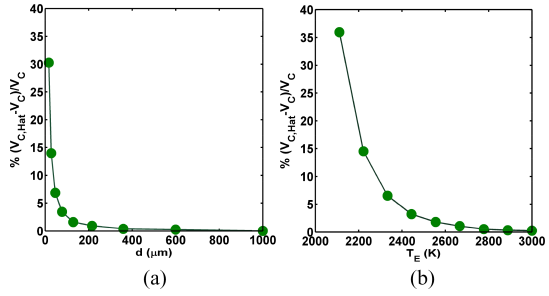

Fig. 4. Comparison of the estimated value of the critical point voltage, V_C, when calculated using the assumptions made by Hatsopoulos, $V_{C,Hat}$, and the actual value of V_C obtained from iteratively solving the problem at different (a) interelectrode distances and (b) emitter temperatures. These results are calculated for typical values of device parameters of $\phi_E = 4.6$ eV, $\phi_C = 4.0$ eV. The radius of the hot spot, r, is assumed to be 100 μm. In part (a), $T_E = 2000$ K and in part (b), $d = 700$ μm.

2) *Current-Voltage Characteristics at the Critical and Saturation Points:* At the saturation point, the maximum motive takes place at the point just outside the emitter ($x_M = 0$ and $J = J_S$). Therefore, $\zeta_E = 0$ and $\zeta(x = d) = \zeta_C = \frac{d-0}{L_D} = (\frac{2\pi m e^2}{\varepsilon_0^2 k_B^3})^{\frac{1}{4}} \frac{J_{E_s}^{1/2} d}{T_E^{3/4}}$, where d is the interelectrode distance. Based on this value of ζ_C, γ_C is interpolated from Fig. 3(a). Following the notations in Fig. 2, with the origin of the x coordinate at the point just outside the emitter, the saturation voltage, V_{sat} is calculated as $(\phi_E - \phi_C - \gamma_C k T_E)$. In calculating the critical point characteristics, it is noted that at this point, the maximum motive occurs just outside the collector ($x_M = d$). Therefore,

$$\gamma_E = \ln(J_{sat}/J_C),\ |\zeta_E| = \left(\frac{0-d}{L_D}\right) = \left(\frac{2\pi m e^2}{\varepsilon_0^2 k_B^3}\right)^{\frac{1}{4}} \frac{J_C^{1/2} d}{T_E^{3/4}}$$

and $\zeta_C = 0$. In order to compute J_C, Hatsopoulus made the assumption that at this point, the distance $|\zeta_E|$ reaches its maximum value (2.554 from Fig. 3(a)). Therefore, J_C can be calculated from this value of $|\zeta_E|$ and then replaced into the Richardson–Dushman equation to evaluate the critical point voltage, V_C. This estimation, as presented in Fig. 4(a) and (b), leads to numerical errors. The value of the V_C calculated using the assumption $|\zeta_E| = 2.554$ is denoted by $V_{C,Hat}$. These values are compared with the V_C values that are obtained using the following proposed method. According to Fig. 4, the approximation made can lead to considerable error in determining the value of V_C.

We propose this method to calculate the exact value of V_C as follows:

a. As a first approximation, J_C and V_C are calculated following the method explained above.
b. Values of $\gamma_E = \ln(J/J_{sat})$ are computed for $10^{-6} < \frac{J}{J_C} < 10^3$.
c. ζ_E is computed for each γ_E, based on their relation from Fig. 3(a).
d. ζ_C is calculated from $\zeta_C = \frac{d-x_M}{x_0} = \frac{d}{x_o} - \zeta_E$. If $\zeta_C < 0$, the maximum motive occurs outside the interelectrode gap and, therefore, the device does not enter the space-charge regime, and operates in the retarding mode. The smallest current that sets $\zeta_C = 0$, is equal to the actual value of J_C.

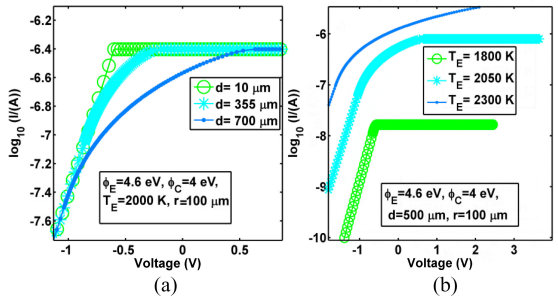

Symbol	$d(\mu m)$	$I_C(d)$	$V_C(d)$	$I_{sat}(d)$	$V_{sat}(d)$	$T_E(K)$	$V_C(T_E)$	$I_C(T_E)$	$V_{sat}(T_E)$	$I_{sat}(T_E)$
○	10	396 nA	−0.6 V	396 nA	−0.6 V	1800	−0.65 V	12 nA	−0.55 V	16.7 nA
✳	355	90 nA	−0.85 V	396 nA	−0.19 V	2050	−1.05 V	64 nA	0.65 V	80 nA
—	700	31 nA	−1.03 V	396 nA	0.63 V	2030	−1.62 V	99 nA	11.8 V	1.7 μA

Fig. 5. The entire *I–V* characteristics and the important boundary points (critical and saturation voltages and currents) were calculated for a wide range of device parameters. The effects of altering (a) the interelectrode gap size and (b) the hot spot temperature on the *I–V* characteristics are included in here. The values of the currents and voltages at the boundary points (critical and saturation points, represented by subscripts "*C*" and "*sat*", respectively), are tabulated in here.

e. V_C is calculated from the Richardson–Dushman equation in the retarding regime: $J = AT_E^2 \exp(-(\phi_C + eV)/kT_E)$.

The value of 10^{-6} for the ratio of currents allows for calculations of actual critical point currents up to 6 orders of magnitude different from the estimated value. If the integrals are not calculated for a wider range, it will not be possible to calculate the exact value of J_C, as large values of γ_E are required in Step c.

3) Output Current-Voltage Characteristics in the Space-Charge Limited Regime: In order to calculate the *I–V* characteristics, the following algorithm is proposed:

a. A procedure similar to the Steps b–d in calculating the critical point is employed, except that the current is chosen within the range of $J_C < J < J_{sat}$.
b. The values of γ_C are computed from the relation between γ_C and ζ_C, as illustrated in Fig. 3(a).
c. The output voltage is calculated from Fig. 2 as $(\phi_E - \phi_C) + k_B T_E (\gamma_E - \gamma_C)$.

Fig. 5(a) and (b) demonstrate the effects of changing the gap width and the emitter's temperature on the *I–V* characteristics of the device, respectively. In the retarding and saturation regimes, the current is determined using the Richardson–Dushman equation with the proper value of the energy barrier that the electron encounters when travelling from the emitter to the collector. On the other hand, in the space-charge limited regime, numerical solutions of equation (2) are used to calculate the characteristics. The entire *I–V* characteristics are eventually obtained by combining the *I–V* curves within these three regions.

B. Non-Uniform Temperature Profile at the Emitter

So far, we have assumed that the temperature is uniform across the illuminated area. This can be a reasonable assumption in the case of the bulk TEC device with large dimensions. However, a detailed analysis of the new generation of TECs with much smaller dimension reveals the presence of temperature gradients. For instance, in a real LITEC device, inspection

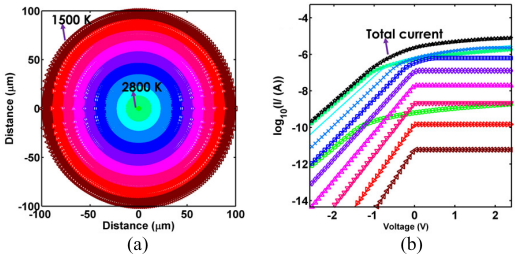

Fig. 6. (a) Temperature profile on the hot spot of the CNT-based LIETC. (b) Contributions of different temperature contour rings to the total current across a hot spot with a radius $r = 200\,\mu\mathrm{m}$.

of the temperature profile reveals an average temperature gradient of several degrees of kelvin over a micrometer at a typical input laser power of 50 mW [26]. Therefore, a uniform temperature profile is not realistic and the influence of the existence of different areas with various temperatures has to be included in the model. In order to model this effect, the circular heat-spot area is divided into different rings with different temperatures ($T(r_n)$), with r_n being the distance of the n$^{\text{th}}$ ring from the center of the beam. Each ring is considered as a thermionic convertor contributing to the overall current. Linear and Gaussian temperature profiles were used to investigate this effect. In the case of a linear temperature profile, $T(r_n) = (T_0 - T_{max})\frac{r}{r_0} + T_{max}$, this leads to an average temperature of $T_{aver} = \frac{1}{\pi r_0^2}\int_0^{r_0} T(r_n) 2\pi r dr = \frac{1}{3}(2T_0 + T_{\max})$, where T_{max} is the maximum temperature, $T_0 = T(r_0)$, and r_0 is the radius of the thermionic emission area (see Fig. 6(a)). The value of T_0 is chosen such that the contribution from the ring at $T = T_0$, is less than 10^{-4} % to the overall current. In the case of a Gaussian temperature distribution, $T(r) = T_{max}\exp(\frac{r^2}{\alpha r_0^2})$, where $\alpha = \ln(T_0/T_{max})$, leads to $T_{aver} = T_{\max}\alpha(-1 + \exp(1/\alpha))$. The contributions of different temperatures when the thermionic emission area is divided into 10 rings are represented in Fig. 6(b). As observed, the average spatial temperature of the spot (2020 K) does not fully represent the thermionic emission behavior of the spot. The reason is the exponential dependence of the emission current on the temperature of the emitter. Therefore, the defining temperature of the device is closer to the maximum temperature than the spatial average temperature. Remarkably, one single temperature cannot fully represent the system in any case. At negative biases, higher-temperature elements with less area contribute predominantly to the current (2710 K with an area of $5.59 \times 10^3\ \mu\mathrm{m}^2$). On the other hand, near the saturation regime, the higher-surface-area rings with relatively lower temperatures dominate. The reason is the high- and low-temperature areas facing the same energy barrier at sufficiently negative biases ($\phi_C + e|V|$). However, in the space-charge limited regime, higher-temperature sectors feel a larger barrier due to the increased space-charge, since they have a higher current density.

III. Experimental Results and Comparisons

A. Experimental Set-Up

Millimeter-long MWCNT forests were grown in a home-built chemical vapor deposition reaction chamber over a highly

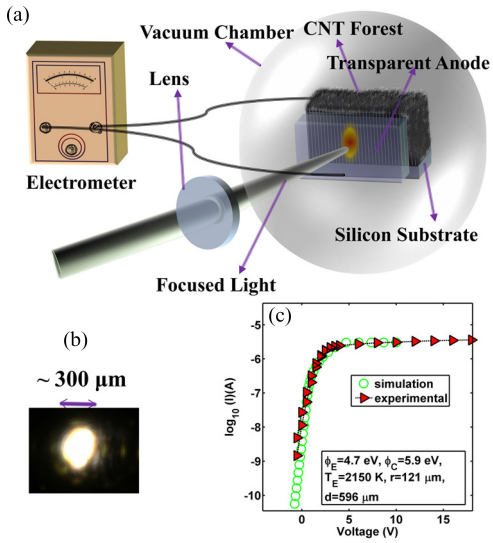

Fig. 7. (a) The schematic of the experimental set-up for *I–V* measurements of a CNT-based LITEC. (b) The incandescent spot on the side-wall of the CNT forest as imaged by a CCD camera. (c) The internal parameters of the LIETC device are obtained by solving the reverse problem and fitting to the experimental results as depicted in the legend of the plot.

p-doped silicon wafer coated with successive layers of 10 nm of Alumina and 1 nm of Iron. Some of the catalysts were patterned to form cubically shaped forests with a base width of 1 mm separated by a distance of ~500 μm. This pattern facilitated the characterization of the illuminated spot on the sidewalls of the CNT forests. CNTs were grown on the catalyst by following a recipe similar to the one used in [13].

The following experimental set-up (see Fig. 7(a)) was adopted for the experiments. The chips containing CNT forests were mounted on a sample holder and placed in a high-vacuum chamber (10^{-5}–10^{-6} torr). The vacuum chamber was equipped with Pirani and cold cathode gauges that allowed the pressure to be monitored within a wide range (10^{3}–10^{-3} and 10^{-2}–10^{-10} torr, respectively). A precision leak valve was used to control the pressure inside the chamber. The CNT sample was used as the cathode and was illuminated on its sidewall through the anode. An indium thin oxide glass slide with 84 % transparency or an 85 % transparent stainless steel mesh were used as the anode. The gap width was set to less than 1 mm. The cathode was surrounded by an open-ended aluminum cube, kept at the same potential as the anode.

The laser was focused on the sidewalls of the CNT forest by means of a lens with a 15-cm focal length. Two manual high precision microactuators were used to move laterally along the width of the forest, allowing one to determine the location of the illuminated spot for characterization purposes. The lens was placed approximately 15 cm away from the anode through a viewport and its exact position was controlled by a high precision motorized microactuator (with a precision of 200 nm) controlled by a computer. Several different types of lasers, including three lasers from Laserglow Technologies (Electra Pro-40 (405 nm), Scorpius-500 (1064 nm) and Hercules (532 nm)) and a 300-mW, 532-nm Green DPSS Laser from Alltech solutions were used. Two optical attenuators and a power reader

were used to adjust the power to the desired value. A charged coupled device (CCD) camera was used to measure the area of the laser spot on the forest (see Fig. 7(b)). The *I–V* characteristics were measured by sweeping from negative (retarding) to positive (collection) voltages using Keithley 6430 and 6517a electrometers. Since the voltage is swept over a wide range in our experiments, the magnitude of current varies dramatically each time (typically from less than 1 pA to $\sim$10 μA for a voltage sweep in the range of $-$4–10 V at $T_E = 2300$ K). At positive biases higher than the saturation voltage of the LITEC device (typically $V = 30$ V to ensure that the saturation regime is properly covered), the current is on the order of tens of μAs.

B. Extracting the Experimental Parameters

As explained in the theoretical section, each regime of operation follows a certain set of equations. Each internal parameter of the LITEC device affects the *I–V* characteristics in a unique way. For instance, increasing the gap width (from Fig. 5) increases the width of the space-charge region while maintaining the same level of saturation current. Raising the emitter's temperature shifts the entire *I–V* curve upwards (increasing current at an exponential rate), while maintaining the intersection of the two tangent lines to the characteristics in the retarding and the saturation modes at a fixed voltage point, $V_m = (\phi_C - \phi_E)/e$. Changing ϕ_E affects the saturation point voltage and current while altering the thermionic emission area's radius (r) shifts the entire curve upward or downward. To distinguish between the alterations caused by T_E or r, it is noted that the former has a more palpable effect in negative biases, while the latter shifts the curve uniformly. Although it seems that each set of parameters will lead to only a unique *I–V* profile, solving for each of the parameters is a challenging problem. In order to solve this reverse problem, a graphical user interface was developed to calculate the *I–V* characteristics based on the proposed procedure, allowing one to select different temperature profiles. Each of the internal parameters are adjusted while their impact on the *I–V* profile is studied in real time. In order to test the uniqueness, a set of reasonable values of internal parameters were chosen in random, the *I–V* curves were generated based on the proposed procedure in the previous section, and the results were used to solve the reverse problem. When the temperature was assumed to be uniform, the reverse problem resulted in unique estimations of the internal parameters, with $\pm$0.1 eV of accuracy for workfunctions, $\sim\pm$ 50 K for T_E and $\sim\pm$ 20 μm for the spot-size radius. The estimation of the inter-electrode distance depends on how deep the device is within the space-charge region. At relatively low *d* values, where V_C is close to V_{sat}, the length of the space-charge region is negligible and, therefore, the impact of the gap width on the *I–V* profile will not be noticeable. Consequently, only an upper bound for *d* can be determined in such cases.

Fig. 7(c) shows the experimental *I–V* characteristics from illumination of the sample (with a stainless steel mesh as the anode) by 40 mW of a 405-nm laser fitted to simulation curves identified by a fixed-gradient temperature profile.

The effective hot spot radius (121 μm) is comparable with the image taken by a CCD camera ($\sim$150 μm). The estimated temperature (2 150 K) when assuming a linear temperature distribution along the hot spot matches closely with the results that our group previously obtained from fitting the incandescence spectra to black body radiation [15], and the estimated workfunction of CNTs (4.7 eV) is consistent with the values obtained by other methods [27].

Since the modelling presented in this paper is based on a 1-D potential profile with infinitely large electrodes, it requires some justification to use this model to extract the parameters of a CNT-based LITEC. In the Appendix section, we show that our 1-D model can effectively capture the experimental conditions by a relatively small error.

Simultaneous measurement of all of these parameters that pertain to a certain experiment in LITEC has not been possible in the past. For instance, in order to measure the workfunction, a common method such as ultraviolet spectroscopy can be employed. However, considering that the exact workfunction depends on the local morphology of the CNTs and the temperature [28], it would be extremely challenging, if not impossible, to have the illuminated spot on the CNTs with exactly the same amount of intensity as that used in the thermionic conversion experiment. Besides the difficulty in determining the actual workfunction, the temperature may vary widely depending on the local density of the CNT forest. For instance, the Richardson–Dushman constants calculated from the thermionic emission data from [19] were in discrepancy with values obtained for metals. This issue was attributed to the extra surface roughness and different surface area for CNTs compared to metals. Furthermore, measurement of the hot-spot area depends on the resolution as well as the bandwidth of the CCD camera used for the measurements. Therefore, the area measured by a CCD camera might be different from the effective area contributing to thermionic emission. However, using *I–V* curves and following the proposed strategy provides a consistent method for determination of the effective area of the hot spot. Moreover, the effective gap width between the electrodes, though being on the same order as its equivalent physical value, can be different due to the collection efficiency of the electrons. The collection efficiency depends on the configuration of the electrodes and the geometry of the structure. As a result, the value of the gap width obtained from fitting to simulation curves can be interpreted as the effective gap width. The magnitude of this parameter is proportional to the physical interelectrode distance divided by the collection coefficient.

IV. Summary

A method was proposed based on the simultaneous solutions of Vlaslov and Poisson equations to calculate the output characteristics of thermionic convertors. The numerical accuracy and the range of applicability of the method were substantially enhanced by applying robust algorithms. It was demonstrated that this method can be employed to solve the reverse problem and calculate the internal parameters, e.g. workfunctions, interelectrode distances, effective areas and temperatures of thermionic convertors. It was shown that the

emergent nanomaterial-based thermionic convertors, though operating on the same overall principles, have some distinct features such as spatially varying workfunctions and the presence of temperature gradients, which require more sophisticated simulation methods to study them. Due to the high stability of the proposed method, a versatile range of parameters can be solved for and, therefore, the method can address the numerical difficulties associated with new thermionic devices. As an example of its application, this method was used to extract the parameters of a LITE conversion device based on CNTs.

APPENDIX
ESTIMATION OF THE INTRODUCED ERROR USING A 1-D MODEL

These steps are followed to calculate the error due to a 1-D model:

1) The lateral movement of electrons does not change the current from that calculated using a 1-D model in retarding and saturation modes of operation. The discrepancy can only arise in the space-charge regime.
2) The electric field in the inter-electrode region in front of every ring is due to two sources: the externally applied bias, and the field due to the presence of electrons, or the space-charge field. In the absence of the space-charge effects, the fields in front of all rings are essentially equal (given that the anode and cathode structures have spatial extents of several millimeters, much larger than the illuminated spot).
3) As described in the modelling section, the space-charge region is identified by the critical point voltage, V_C, and the saturation point voltage, V_{sat}. Under the foregoing experimental conditions, only a small number of the rings enter the space-charge dominated regime, and for only a small portion of their entire IV characteristics. For instance, in the case of the lowest-temperature ring (1500 K), V_C and V_{sat} coincide at 1.2001 V (as calculated using the prosed method in the paper), signifying that this ring does not enter the space-charge regime at all. Similar calculations reveal that the device enters the space-charge regime of operation at temperatures higher than $1900\ K$, with $V_C = 1.0654$ V and $V_{sat} = 1.3651$ V. Therefore, the 1-D approximation is fully valid for about $3/4$ of the rings. For the remaining $1/4$ of the rings, the approximation is not valid for a very short range of applied biases (for instance for 0.3 V of the 40 V range of voltage sweep).
4) The width of the space-charge regime is narrower in our LITE device, where the emission spot is finite in size, compared to the traditional case of an "infinitely-wide" hot electrode. The reason is that the space charge density in the transverse direction decreases with distance from the axis (of the rings), since electrons are only fired from the finite-size hot spot. In other words, as the electron beam travels away from the hot spot, its diameter increases and its total charge is distributed over a wider area than the size of the hot spot; the amount of charge directly in front of the hot spot is thus effectively reduced. Therefore, for instance, we would expect that the width of the space-charge limited regime at 1900 K be less than 0.3 V; an estimation of how much lower it should be is presented in the next point.
5) The estimation of the maximum change (to the infinitely-wide emission spot case) can be obtained as follows: in our experimental case, a hot spot with area $A(0) = \pi R^2$ and average electron density $n(0)$, expands to an approximate area of $A(x) = \pi(R + v_{\rm th} \times t_{tof})^2$ with its electron density diluted to $n_2(x) = n_1(x) \times A(0)/A(x)$, where $v_{\rm th} = (2k_B T/m)^{1/2}$, t is the average time of flight of the electrons ($t = \frac{x}{\langle v_x \rangle}$), $\langle v_x \rangle$ is the average velocity of electrons along the x direction and $n_1(x)$ is the density of electrons at position x in the 1-D case (uniform temperature and infinitely large electrodes) that can be calculated using equation 2 and Fig. 3. On the other hand, in the 1-D case, a portion of the hot spot with area $A(0)$ maintains its surface area due to the charge migration from the adjacent regions and its electron density, $n_1(x)$, varies along the gap distance according to equation 2. The potential of a uniform circular surface charge distribution, $\sigma(x) = n(x)dx$ at a distance x from the center of the circle can be easily calculated as $V = \frac{\sigma(x)}{2\varepsilon_0}(\sqrt{R^2 + x^2} - x)$. Therefore, the fractional change in the potential barrier at the emitter due to dilution of electron density at point x can be calculated as $\frac{n_2(x)dx}{2\varepsilon_0}(\sqrt{(R + v_{\rm th} \times t)^2 + x^2} - x)$. This potential was numerically integrated along the gap distance to calculate the overall change in the emitter's potential due to dilution of the electron density because of the expansion of the beam. The same procedure was employed to calculate the generated potential at the emitter in the 1-D case. This led to a maximum introduced error of 15 % in the resulting potential occurring at the bias point, $V = 1.2$ V at 1500 K.
6) In order to include the influence of the electron mixing between adjacent rings (the influence of the space charge of electrons emitted by all other rings, including the dilution of the electrons of the ring in question itself), the solution of the Laplace equation in spherical coordinates with azimuthal symmetry involving Legendre functions of the first kind [28], was used to include the introduced potential at off-axis points resulting from dispersing rings. Not including the mixing of electrons between the adjacent rings led to a maximum error of 12 % in the ring's own potential at the emitter, 7 % of error in the potential of the adjacent ring and 4 % in the next one (the impact on the subsequent ring is less than 1 %).
7) We can thus infer that the width of the space-charge limited regime of operation is roughly $12 + 7 + 4 = 23\,\%$ of the width predicted by the 1-D model due to mixing of the electrons (for instance instead of $0.3\,V$, it is $0.3 \times (1 - 23\,\%) = 0.23$ V wide).

Based on these observations, for the device studied experimentally here, the error introduced in the simulations due to the 1-D nature of the model occurs in only 2 % of the data points.

REFERENCES

[1] F. Guthrie, "On a relation between heat and static electricity," *Lond. Edinb. Dublin Philosoph. Mag. J. Sci.*, vol. 46, pp. 257–266, 1873.

[2] A. B. Hargadon and Y. Douglas, "When innovations meet institutions: Edison and the design of the electric light," *Administ. Sci. Quart.*, vol. 46, no. 3, pp. 476–501, Sep. 2001.

[3] O. W. Richardson, *Thermionic Emission From Hot Bodies*. Wexford, Ireland: Wexford College Press, 2003.

[4] T. L. Westover, A. D. Franklin, B. A. Cola, T. S. Fisher, and R. G. Reifenberger, "Photo- and thermionic emission from potassium-intercalated carbon nanotube arrays," *J. Vac. Sci. Technol. B Microelectron. Nanometer Struct.*, vol. 28, no. 2, pp. 423–434, 2010.

[5] V. Robinson, T. Fisher, J. Michel, and C. Lukehart, "Work function reduction of graphitic nanofibers by potassium intercalation," *Appl. Phys. Lett.*, vol. 87, p. 061501, Aug. 2005.

[6] A. H Khoshaman, H. D. Fan, and A. Nojeh, "Improving the efficiency of light induced thermionic energy conversion of carbon nanotubes by potassium intercalation," presented at the 97th Can. Chem. Conf. Exhib., Vancouver, BC, Canada, 2014.

[7] G. L. Bilbro, J. R. Smith, and R. J. Nemanich, "Theory of space charge limited regime of thermionic energy converter with negative electron affinity emitter," *J. Vac. Sci. Technol. B Microelectron. Nanometer Struct.*, vol. 27, pp. 1132–1141, 2009.

[8] J. W. Schwede, I. Bargatin, D. C. Riley, B. E. Hardin, S. J. Rosenthal, Y. Sun, F. Schmitt, P. Pianetta, R. T. Howe, Z.-X. Shen, and N. A. Melosh, "Photon-enhanced thermionic emission for solar concentrator systems," *Nature Mater.*, vol. 9, no. 9, pp. 762–767, Sep. 2010.

[9] S. Meir, C. Stephanos, T. H. Geballe, and J. Mannhart, "Highly-efficient thermoelectronic conversion of solar energy and heat into electric power," *J. Renew. Sustainable Energy*, vol. 5, no. 4, art. no. 043127, pp. 1–15, Jul. 2013.

[10] J. H. Lee, I. Bargatin, T. O. Gwinn, M. Vincent, K. A. Littau, R. Maboudian, Z.-X. Shen, N. A. Melosh, and R. T. Howe, "Microfabricated silicon carbide thermionic energy converter for solar electricity generation," in *Proc. IEEE 25th Int. Conf. Micro Electro. Mech. Syst.*, 2012, pp. 1261–1264.

[11] A. Khoshaman, H. D. E. Fan, A. Koch, G. Sawatzky, and A. Nojeh, "Thermionics, thermoelectrics, and nanotechnology: New possibilities for old Ideas," *IEEE Nanotechnol. Mag.*, vol. 8, no. 2, pp. 4–15, Jun. 2014.

[12] F. Jin, Y. Liu and C. M. Day, "Thermionic emission from carbon nanotubes with a thin layer of low work function barium strontium oxide surface coating," *Appl. Phys. Lett.*, vol. 88, no. 16, p. 163116, 2006.

[13] P. Yaghoobi, M. V. Moghaddam, and A. Nojeh, "Solar electron source and thermionic solar cell," *AIP Adv.*, vol. 2, no. 4, pp. 042139-1–042139-12, Nov. 2012.

[14] S. F. Adams, "Solar thermionic space power technology testing: A historical perspective," *AIP Conf. Proc.*, vol. 813, no. 1, pp. 590–597, Jan. 2006.

[15] P. Yaghoobi, M. V. Moghaddam, and A. Nojeh, "Heat trap': Light-induced localized heating and thermionic electron emission from carbon nanotube arrays," *Solid State Commun.*, vol. 151, no. 17, pp. 1105–1108, Sep. 2011.

[16] G. N. Hatsopoulos and E. P. Gyftopoulos, *Thermionic Energy Conversion*, vol. 1. Cambridge, MA, USA: MIT Press, 1973.

[17] G. N. Hatsopoulos and E. P. Gyftopoulos, *Thermionic Energy Conversion—Vol. 2: Theory, Technology, and Application*. Cambridge, MA, USA: MIT Press, 1979.

[18] S. Suzuki, Y. Watanabe, Y. Homma, S. Fukuba, S. Heun, and A. Locatelli, "Work functions of individual single-walled carbon nanotubes," *Appl. Phys. Lett.*, vol. 85, no. 1, pp. 127–129, Jul. 2004.

[19] M. Grujicic, G. Cao, and B. Gersten, "Enhancement of field emission in carbon nanotubes through adsorption of polar molecules," *Appl. Surf. Sci.*, vol. 206, nos. 1–4, pp. 167–177, Feb. 2003.

[20] A. Maiti, J. Andzelm, N. Tanpipat, and P. von Allmen, "Effect of adsorbates on field emission from carbon nanotubes," *Phys. Rev. Lett.*, vol. 87, no. 15, p. 155502, 2001.

[21] G. Zhou, W. Duan, and B. Gu, "Electronic structure and field-emission characteristics of open-ended single-walled carbon nanotubes," *Phys. Rev. Lett.*, vol. 87, no. 9, p. 095504, Aug. 2001.

[22] C. R. Crowell, "The richardson constant for thermionic emission in Schottky barrier diodes," *Solid-State Electron.*, vol. 8, no. 4, pp. 395–399, Apr. 1965.

[23] U. S. Inan and M. Golkowski. (2010). *Principles of Plasma Physics Engineers and Scientists*. Cambridge, U.K.: Cambridge Univ. Press. [Online]. Available: http://www.cambridge.org/us/academic/subjects/engineering/electromagnetics/principles-plasma-physics-engineers-and-scientists.

[24] M. E. Kiziroglou, X. Li, A. A. Zhukov, P. A. J. de Groot, and C. H. de Groot, "Thermionic field emission at electrodeposited Ni–Si schottky barriers," *Solid-State Electron.*, vol. 52, no. 7, pp. 1032–1038, Jul. 2008.

[25] J. Orloff, *Handbook of Charged Particle Optics*, 2nd ed. Boca Raton, FL, USA: CRC Press, 2009.

[26] M. Chang, M. V. Moghaddam, A. Khoshaman, M.S. M. Ali, M. Dahmardeh, K. Takahata, and A. Nojeh. (2013). High temperature gradient in a conductor: carbon nanotube forest under the 'heat trap' condition. Nashville, TN, USA. presented at the 57th Int. Conf. Electron. Ion, Photon Beam Technol. Nanofabrication. [Online]. Available: http://eipbn.omnibooksonline.com/data/papers/2013/P11–08.pdf#page = 1 (2pp).

[27] P. Liu, Y. Wei, K. Jiang, Q. Sun, X. Zhang, S. Fan, S. Zhang, C. Ning, and J. Deng, "Thermionic emission and work function of multiwalled carbon nanotube yarns," *Phys. Rev. B*, vol. 73, no. 23, p. 235412, Jun. 2006.

[28] P. Liu, Q. Sun, F. Zhu, K. Liu, K. Jiang, L. Liu, Q. Li, and S. Fan, "Measuring the work function of carbon nanotubes with thermionic method," *Nano Lett.*, vol. 8, no. 2, pp. 647–651, Feb. 2008.

Authors' photograph and biographies not available at the time of publication.